International journal of imaging science and engineering

ISSN: 1934--9955 www.ijise.net

Vol-20 Issue-01 Mar 2025

POWER ENHANCEMENT FOR GRID CONNECTED WIND TURBINE ENERGY SYSTEM

Mr.N.Chathru[1], G. Nandini[2], Prithvi Roshan[3], T.Uma Shankar[4], R. Tarun[5]

[1] Assistant Professor, Dept. of EEE, Sri Indu College of Engineering and Technology, Hyderabad,
[2 3 4] Research Student, Dept. of EEE Sri Indu College of Engineering and Technology, Hyderabad

---

***Abstract*—A comprehensive control of a wind turbine system connected to an industrial plant is discussed in this paper, where an algorithm has been developed allowing a control structure that utilizes a four-leg inverter connected to the grid side to inject the available energy, as well as to work as an active power filter mitigating load current disturbances and enhancing power quality. A four-wire system is considered with three-phase and single-phase linear and nonlinear loads. During the connection of the wind turbine, the utility-side controller is designed to compensate the disturbances caused in presence of reactive, nonlinear, and/or unbalanced single- and intra-phase loads, in addition to providing active and reactive power as required. When there is no wind power available, the controller is intended to improve the power quality using the dc-link capacitor with the power converter attached to the grid. The main difference of the proposed methodology with respect to others in the literature is that the proposed control structure is based on the conservative power theory decompositions. This choice provides decoupled power and current references for the inverter control, offering very flexible, selective, and powerful functionalities. Real-time software benchmarking has been conducted in order to evaluate the performance of the proposed control algorithm for full real-time implementation. The control methodology is implemented and validated in hardware-in-the-loop based on the real time simulator "Opal-RT" and a TMSF28335 DSP microcontroller. The results corroborated our power quality enhancement control and allowed to exclude passive filters, contributing to a more compact, flexible, and reliable electronic implementation of a smart-grid based control.**

***Index Terms*—Conservative power theory (CPT), four-leg voltage source converter (VSC), hardware-in-the-loop (HIL), permanent magnet synchronous generator (PMSG), power quality.**

I. Introduction

THE GLOBAL capacity of installed wind turbines has rapidly increased in the last few years, by 2013 there were about 300 GW of installed wind capacity [1]. There have been tremendous developments in the wind turbine industry supporting this energy source as a mainstream renewable resource, with competitive costs in $/kWh when compared to traditional fossil fuel power plants. This development is due to the advancement in electrical generators and power electronics. The main issue with renewable energy is that the power is not always available when it is needed.

With the increase of power production of renewable resources, utility integration has been developed and implemented and power electronic inverters are used to control active/reactive power, frequency, and to support grid voltage during faults and voltage sags [2]–[4].

Several control approaches have been introduced in the literature for wind turbine in standalone and grid connected systems [5], [6]. The machine side controllers are designed to extract maximum power point from wind using hill-climbing control, fuzzy-based, and adaptive controllers [7], most of the time based on field-oriented or vector control approach. The grid side controllers are designed to ensure active and reactive power is delivered to the grid [8], [9].

In order to allow the theoretical framework, different power theories have been proposed and implemented in electrical power systems to analyze current and voltage components, such as the instantaneous power (PQ) theory for a three-phase system made by Akagi [10]. In PQ theory, the three-phase is transformed into a two-phase reference frame in order to extract active and reactive components in a simplified manner. A three-phase power theory in a broader perspective has been introduced, known as the conservative power theory (CPT) [11], where the current and voltage components are derived in the three-phase form, without requiring any reference-frame transformation [12]. The performance of these theories has been compared in [13] and [14].

This paper proposes a control structure in three-phase four-wire systems that provide more functionality to the grid-side converter of a wind turbine system using the CPT as an alternative to generating different current references for selective disturbances compensation, where both single- and three-phase loads are fed. Three-phase, four-wire inverters have been realized using conventional three-leg converters with "split-capacitor" or four-leg converters [15], [16]. In a three-leg conventional converter, the ac neutral wire is directly connected to the electrical midpoint of the dc bus. In four-leg converter, the ac neutral wire connection is provided through the fourth switch leg. The "four-leg" converter topology has better controllability

Manuscript received May 15, 2016; revised October 3, 2016; accepted December 18, 2016. Date of publication January 24, 2017; date of current version May 18, 2017. Paper 2016-IACC-0422.R1, presented at the 2015 Industry Applications Society Annual Meeting, Addison, TX, USA, Oct. 18–22, and approved for publication in the IEEE Transactions on Industry Applications by the Industrial Automation and Control Committee of the IEEE Industry Applications Society.

A. S. Bubshait, A. Mortezaei, and M. G. Simo˜es are with the Division of Electrical Engineering, Department of Electrical Engineering and Computer Science, Colorado School of Mines, Golden, CO 80401 USA (e-mail: abubshai@mines.edu; amorteza@mines.edu; msimoes@mines.edu).

T. D. C. Busarello is with the Federal University of Santa Catarina, Blumenau SC 88040-900, Brazil (e-mail: tiago_curi@yahoo.com.br).

Color versions of one or more of the figures in this paper are available online at http://ieeexplore.ieee.org.

Digital Object Identifier 10.1109/TIA.2017.2657482

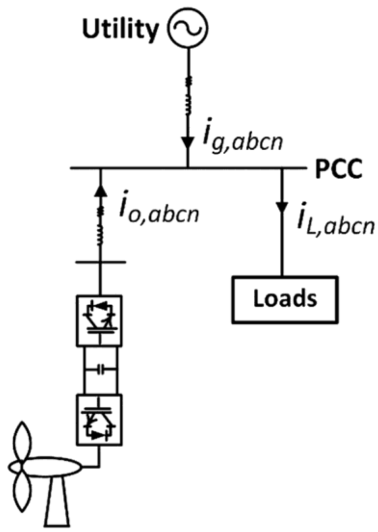

Fig. 1. Single line diagram of the addressed industrial system with wind turbine system.

than the "split-capacitor" converter topology [17]–[19]. The considered system consists of single- and three-phase linear and nonlinear (balanced and unbalanced) loads. The CPT is used to identify and to quantify the amount of resistive, reactive, unbalanced, and nonlinear characteristics of a particular load under different supply voltages condition for four-wire system. This paper is the journal version of our presented work in the 2015 Industry Applications Society (IAS) Annual Meeting [20].

The organization of the paper is as follows. Section II presents the utility-connected wind turbine system considered in this paper. In Section III, a brief review of the CPT for three-phase circuits is presented. Section IV presents the control design of the back-to-back converter system. Section V is dedicated to the experimental verification of the proposed control structure through a real-time hardware-in-the-loop (HIL) setup. Finally, the conclusion of this paper is presented in Section VI.

II. System Configuration

Fig. 1 shows a diagram of a utility connected industrial system addressed in this paper. The structure of the power converter used in the wind turbine system is a back-to-back converter with a permanent magnet synchronous generator (PMSG) connected to the same bus with the loads. The loads are a combination of linear and highly inductive loads causing harmonics at the point of common coupling (PCC).

The model of the wind turbine system considered in this paper is described in [21]. The generator of the system is based on the PMSG. The model of the PMSG used in this paper is presented in [20].

III. Conservative Power Theory

The CPT, proposed by [11], decomposes the power and current in the stationary frame, according to terms directly related to electrical characteristics, such as average power transfer, reactive energy, unbalanced loads and nonlinearities. Assuming a generic poly-phase circuit under periodic operation (period T), where ($\underline{v}$) and ($\underline{i}$) are, respectively, the voltage and current vectors, and ($\hat{\underline{v}}$) is the unbiased integral of the voltage vector measured at a given network port (phase variables are indicated with subscript "m"), the CPT authors define [13].

1) Instantaneous active power

$$p(t) = \underline{v} \cdot \underline{i} = \sum_{m=1}^{M} v_m\, i_m. \tag{1}$$

2) Instantaneous reactive energy

$$w(t) = \hat{\underline{v}} \cdot \underline{i} = \sum_{m=1}^{M} \hat{v}_m\, i_m. \tag{2}$$

The corresponding average values of (1) and (2) are the active power and reactive energy defined in (3) and (4), respectively as follows:

$$P = \bar{p} = \langle \underline{v}, \underline{i} \rangle = \frac{1}{T}\int_0^T \underline{v} \cdot \underline{i}\, dt = \sum_{m=1}^{M} P_m, \tag{3}$$

$$W = \bar{w} = \langle \hat{\underline{v}}, \underline{i} \rangle = \frac{1}{T}\int_0^T \hat{\underline{v}} \cdot \underline{i}\, dt = \sum_{m=1}^{M} W_m. \tag{4}$$

The phase currents are decomposed into three current components as follows.

Active phase currents are defined by

$$i_{am} = \frac{\langle v_m, i_m \rangle}{\|v_m\|^2}\, v_m = \frac{P_m}{V_m^2}\, v_m = G_m\, v_m, \tag{5}$$

where (G_m) is the equivalent phase conductance.

Reactive phase currents are given by

$$i_{rm} = \frac{\langle \hat{v}_m, i_m \rangle}{\|\hat{v}_m^2\|}\, \hat{v}_m = \frac{W_m}{\hat{V}_m^2}\, \hat{v}_m = B_m\, \hat{v}_m, \tag{6}$$

where (B_m) is the equivalent phase reactivity.

Void phase currents are the remaining current terms

$$i_{vm} = i_m - i_{am} - i_{rm}, \tag{7}$$

where they convey neither active power nor reactive energy.

The active and reactive phase currents can be further decomposed into balanced and unbalanced terms.

The balanced active currents have been defined as

$$\underline{i}_{am}^{b} = \frac{\langle \underline{v}, \underline{i} \rangle}{\|\underline{v}^2\|}\, \underline{v}_m = \frac{P}{V^2}\, \underline{v}_m = G^b\, \underline{v}_m, \tag{8}$$

and such currents represent the minimum portion of the phase currents, which could be associated with a balanced equivalent circuit, responsible for conveying the total active power (P) in the circuit, under certain voltage conditions.

The balanced reactive currents have been defined as

$$\underline{i}_{rm}^{b} = \frac{\langle \hat{\underline{v}}, \underline{i} \rangle}{\|\hat{\underline{v}}^2\|}\, \hat{\underline{v}}_m = \frac{W_r}{\hat{V}^2}\, \hat{\underline{v}}_m = B^b\, \hat{\underline{v}}_m, \tag{9}$$

and they represent the minimum portion of the phase currents, which could be associated with a balanced equivalent circuit, responsible for conveying the total reactive energy (W) in the circuit.

The imbalanced active currents are calculated by difference between (5) and (8)

$$i_{am}^{u} = i_{am} - i_{am}^{b} = (G_m - G^b)\, v_m. \tag{10}$$

International journal of imaging science and engineering

ISSN: 1934--9955 www.ijise.net
Vol-20 Issue-01 Mar 2025

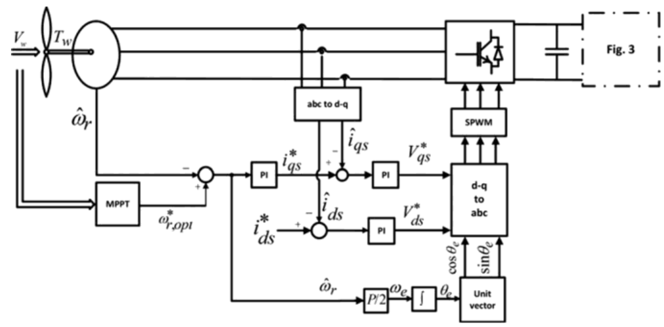

Fig. 2. Control scheme of machine side converter.

TABLE I
PMSG PARAMETERS AND WIND TURBINE SPECIFICATIONS

Parameters	Values
Stator resistance, R_s	0.672 Ω
d-axis leakage inductance, L_d	13.74 mH
q-axis leakage inductance, L_q	13.74 mH
Flux linkage, ψ_m	2.39 Wb
Number of poles of machines, P	24
Voltage	500 V
Nominal output power of wind turbine	10 kW
Base wind speed	10 m/s
Base rotor speed	200 r/min

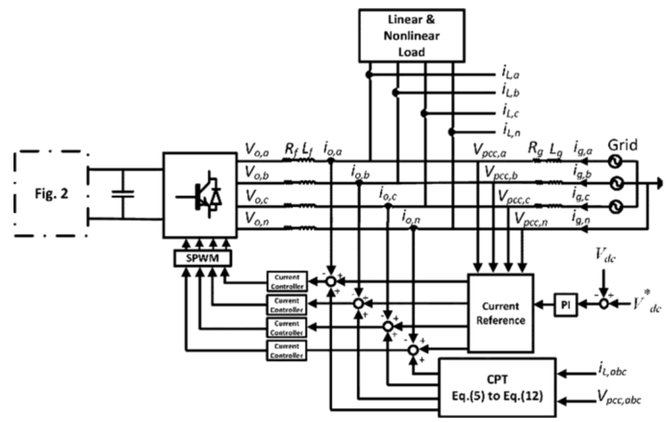

Fig. 3. Control scheme of a grid-side converter.

In the same way, the imbalanced reactive currents are

$$i^u_{rm} = i_{rm} - i^b_{rm} = (B_m - B^b)\hat{v}_m. \quad (11)$$

Thus, the total imbalance phase current vector is defined as

$$i^u_m = i^u_{am} + i^u_{rm}. \quad (12)$$

The current vector can be given as

$$\underline{i} = \underline{i}^b_a + \underline{i}^b_r + \underline{i}^u_a + \underline{i}^u_r + \underline{i}_v. \quad (13)$$

IV. CONTROL DESIGN

A. Machine Side Controller

The purpose of the machine side converter is to track the optimum point of the rotor to extract the maximum power existing in the turbine. For a given wind turbine, the maximum power occurs at the maximum power coefficient of the turbine [22]. For a given wind speed, there is an optimum rotor speed that gives the optimum tip speed ratio

$$\lambda_{\text{opt}} = \frac{R_w \ \omega_{w,\text{opt}}}{v_w}. \quad (14)$$

By knowing the tip speed ratio of the wind turbine, one can extract the maximum power from the rotor by calculating the optimum rotor speed as

$$\omega_{w,\text{opt}} = \frac{v_w \lambda_{\text{opt}}}{R_w}. \quad (15)$$

Then, this optimum rotor reference is subtracted from the measured rotor speed to produce the speed error. As shown in Fig. 2, a rotor speed controller is designed to generate the quadrature current reference to the internal current controller. The direct current reference in this paper is set to zero. The detail of the controller design procedure is presented in [23]. The parameters and values of the grid-side system and the load are illustrated in Table I.

B. Grid-Side Controller

In this section, the current-controlled voltage source inverter is designed and modeled. The control scheme for the four-leg grid-side inverter is shown in Fig. 3.

Fig. 3 illustrates the schematic diagram of the grid-tied four-leg inverter unit, consisting of a four-leg voltage source converter (VSC) and the network load that are connected to the distribution network at PCC. The inductance of the filter is L_f and R_f is the ohmic loss of the inductor. The machine side converter of Fig. 2 is connected in parallel with the VSC dc-link capacitor C_{dc}. It is shown that the grid-side inverter unit is controlled in an *abc*-reference frame. v_{pcc} is dictated by the grid representing the PCC/load voltage. The control objective is to allow the wind source to inject its available energy, as well as to work as an active power filter for improving power quality based on CPT functionalities. Fig. 4 shows the circuit, containing both balanced and unbalanced linear and nonlinear loads. The parameters and values of the grid-side system and the load are illustrated in Table II.

The inverter unit control system consists of two feedback control loops [14]. The first loop demonstrated in Fig. 5 is a fast loop controlling the output current, showing that $i_{o,\text{abcn}}$ can rapidly track their respective reference commands $i^*_{o,\text{abcn}}$, while $i^*_{o,n}$ is determined as $i^*_{o,n} = -(i^*_{o,a} + i^*_{o,b} + i^*_{o,c})$. The outer loop depicted in Fig. 8 is a slower loop regulating the dc-link voltage. The dc-link keeps the power balance between the power which is delivered to the system in the output of the inverter and the power in the dc-link. The desired inverter output current is the summation of the active current provided from the wind (i_{active}) and the compensation of unwanted load current disturbances delivered by the CPT technique. The block diagram of the system in the "*s*" plane shown in Fig. 5 is designed in an *abc* frame based on the classical frequency response analysis method.

Consider the grid-tied four-leg inverter of Fig. 3 and the current control loop block diagram of Fig. 5; the dynamics

ISSN: 1934--9955 www.ijise.net
Vol-20 Issue-01 Mar 2025

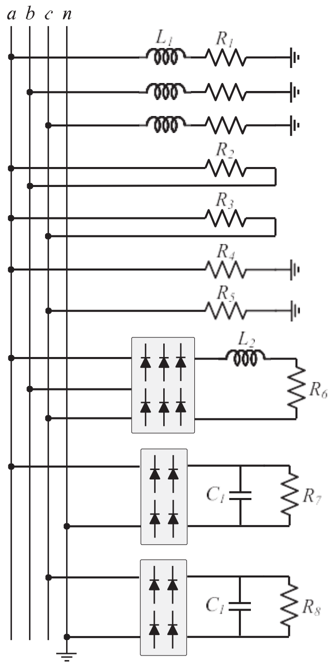

Fig. 4. Schematic diagram of the configurable load in Fig. 3.

TABLE II
GRID SIDE SYSTEM AND LOAD PARAMETERS

Parameters	Values
Nominal grid pick phase voltage, v_{pcc}	180 V
Grid frequency, f	60 Hz
Switching frequency, f_s	12 kHz
Output filter inductor, L_f	10 mH
Output filter resistor, R_f	0.1 Ω
DC link voltage refrence, V_{dc}	1000 V
DC-link capacitor, C_{dc}	5 mF
Grid inductor, L_g	3 mH
Grid resistor, R_g	1 Ω
Load inductor, L_1	30 mH
Load inductor, L_2	4 mH
Load capacitor, C_1	220 μF
Load resistor, R_1	1 Ω
Load resistor, R_2	80 Ω
Load resistor, R_3	35 Ω
Load resistor, R_4	30 Ω
Load resistor, R_5	40 Ω
Load resistor, R_6	200 Ω
Load resistor, R_7	150 Ω
Load resistor, R_8	200 Ω

of the ac-side currents $i_{o,abcn}(t)$ are described by (16) and (17). Equation (16) represents a system in which $i_{o,abcn}(t)$ are the state variables, $v_{o,abcn}(t)$ are the control inputs, and $v_{pcc,abcn}(t)$ are the disturbance inputs. Based on (17), the control input $v_{o,abcn}(t)$ are proportional to, and can be controlled by, the modulating signal $m_{o,abcn}(t)$. The transfer function of the current control scheme, $G_i(s)$, is determined as in (18). The first step to perform the controller design is to obtain the open-loop current transfer function $G_{oi}(s)$ as expressed in (19) with $C_i(s)$ the controller of the current control loop, consisting of a lag compensator as (20), where the parameters of

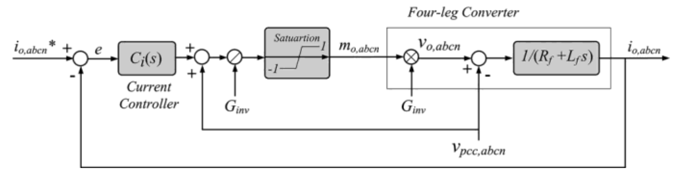

Fig. 5. Block diagram of the current control loop.

ω_z , ω_p , and k_c are the zero, pole, and the gain of the compensator, respectively. Furthermore, the voltage feed-forward compensation is employed to mitigate the dynamic couplings between the four-leg inverter and the ac system, enhancing the disturbance rejection capability of the converter system [24]

$$L_f \frac{di_{o,abcn}(t)}{dt} + R_f i_{o,abcn}(t) = v_{o,abcn}(t) - v_{pcc,abcn}(t). \tag{16}$$

$$v_{o,abcn}(t) = G_{inv}\, m_{o,abcn}(t) = \frac{V_{dc}}{2}\, m_{o,abcn}(t). \tag{17}$$

$$G_i(s) = \frac{i_{o,abcn}(s)}{v_{o,abcn}(s)} = \frac{1}{L_f s + R_f}. \tag{18}$$

$$G_{oi}(s) = \frac{C_i(s)}{R_f + sL_f}, \tag{19}$$

$$C_i(s) = \frac{k_c\left(1 + {}^{s}/_{\omega_z}\right)}{1 + {}^{s}/_{\omega_p}}. \tag{20}$$

For DSP implementation of the control system, in the next step, it is suggested to convert the functions of continuous plane "s" to the discrete plane "z". The Plant transfer function in z-domain is obtained by means of the z-transformation. The z-transformation of a transfer function in s-domain, combined to a zero-order holder, is given by (21). Transformation is made using the relation $z = e^{s.T_a}$. So, $G_i(z)$ can be defined as follows [24]:

$$G_i(z) = Z\left(\frac{1 - e^{-s.T_a}}{s} G_i(s)\right). \tag{21}$$

$$G_i(z) = \left(1 - z^{-1}\right) Z\left(\frac{G_i(s)}{s}\right). \tag{22}$$

To allow the use of the frequency response method design, the conversion of $G_i(z)$ transfer function from "z" plane to "w" plane is performed using the bilinear transform shown in (23)

$$z = \frac{1 + \frac{T_a}{2} w}{1 - \frac{T_a}{2} w}. \tag{23}$$

From where comes

$$G_i(w) = \frac{-0.0041w + 100}{w + 10}. \tag{24}$$

Fig. 6 presents a comparison between the frequency response of system transfer function $G_i(s)$, and digitalized plant $G_i(w)$. It is noticeable that the frequency response presents conformity

ISSN: 1934--9955 www.ijise.net
Vol-20 Issue-01 Mar 2025

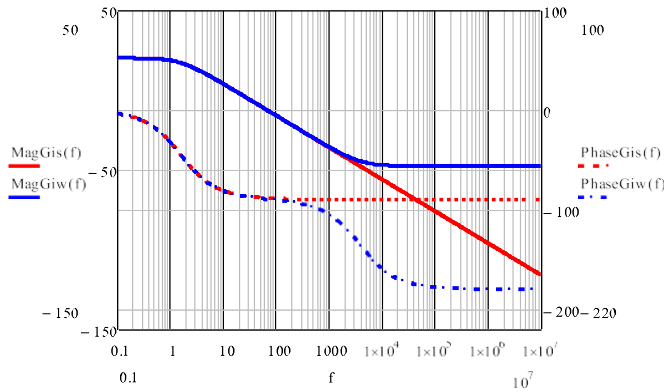

Fig. 6. Gain and the phase of the current control plant in both "s" and "w" planes.

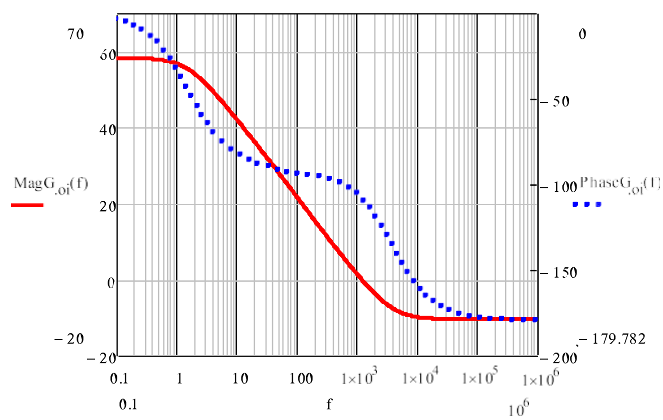

Fig. 7. Bode plot of the open-loop current transfer function.

up to 3 kHz, when the phase error goes by substantial caused by the zero added because of the digitalization process.

The crossover frequency of the current controller is chosen to be one-tenth of switching frequency. For f_{ci} = 1.2 kHz, ϕ_{PMi} = 72°, and $f_z = f_{ci}/10$ = 120 Hz, the rest of parameters in (20) are calculated as f_p = 106.6 Hz and k_c = 80.88. The frequency response of the open-loop transfer function is illustrated in Fig. 7. It can be seen that at crossover frequency, the open loop gain of 0 dB and the phase margin of 72° are obtained.

The output current behavior of the grid-tied four-leg inverter can be described by (25). It can be seen that the output current only depends on the reference current. In other words, under the feed-forward compensation, the converter system is equivalent to an independent current source as viewed by the ac system

$$i_{o,abcn}(s) = \frac{C_i(s)}{L_f s + R_f + C_i(s)} i^*_{o,abcn}(s). \qquad (25)$$

For digital implementation of the control system in the z-domain, the controller of (20) is discretized by the bilinear transform with a sampling time of T_s that is also the switching period [24]. Therefore, the controller transfer function $C_i(z)$ can be expressed as (26)

$$C_i(z) = \frac{72.1z - 67.7}{z - 0.94}. \qquad (26)$$

The current reference, $i_{\text{active,abc}}$, is used to inject the active power delivered from the wind through the inverter. The waveform of the active current reference is defined from the fundamental component of the measured load voltage, $v^f_{\text{pcc,abc}}$, configuring sinusoidal current. Therefore, the active current is a pure sinusoidal current, in phase with the fundamental component of the instantaneous load voltage. Dimensioning of the dc-link voltage controller is determined by the transfer function between the defined current reference and the dc-link voltage.

From power balance of the inverter terminal, we have

$$P_{ac} + P_{\text{wind}} + P_{\text{cap}} = 0. \qquad (27)$$

$$\frac{3}{2} v^f_{\text{pcc,abc}} i_{\text{active,abc}} + V_{dc} I_{dc} + V_{dc}\, i_{\text{capacitor}} = 0. \qquad (28)$$

where $i_{\text{capacitor}}$ is the dc-link capacitor current and 3/2 factor comes from the average ac power flow using peak values and $v^f_{\text{pcc,abc}}$ represents the fundamental component of the PCC voltage.

From (28) the current through the capacitor is

$$i_{\text{capacitor}} = -\left(\frac{3 v^f_{\text{pcc,abc}} i_{\text{active,abc}}}{2V_{dc}} + I_{dc}\right). \qquad (29)$$

The same current in terms of voltage across the capacitor is given by

$$C_{dc}\frac{dV_{dc}}{dt} = i_{\text{capacitor}}. \qquad (30)$$

From (29) and (30), the differential equation for the dc-link voltage becomes

$$\frac{dV_{dc}}{dt} = -\frac{1}{C_{dc}}\left(\frac{3 v^f_{\text{pcc, abc}} i_{\text{active,abc}}}{2V_{dc}} + I_{dc}\right). \qquad (31)$$

Based on (31) the dc voltage is regulated by controlling the active current $i_{\text{active,abc}}$. The block diagram of the dc voltage control loop is shown in Fig. 8. The dc-link voltage controller $C_{vdc}(s)$ is multiplied by −1 to compensate for the negative sign of dc bus voltage dynamics. We will select the bandwidth of dc voltage loop to be less than two orders of magnitude smaller than that of the current loop.

Therefore, the closed current loop can be assumed ideal for design purposes and replaced by unity. The transfer functions of dc-link voltage control scheme, $G_{vdc}(s)$, is presented in (32). The open-loop transfer functions of the dc voltage control loop, $G_{ovdc}(s)$, is presented in (33) with $C_v(s)$ the controller

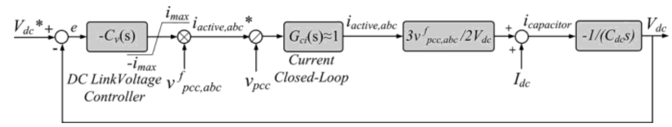

Fig. 8. Block diagram of the dc voltage control loop.

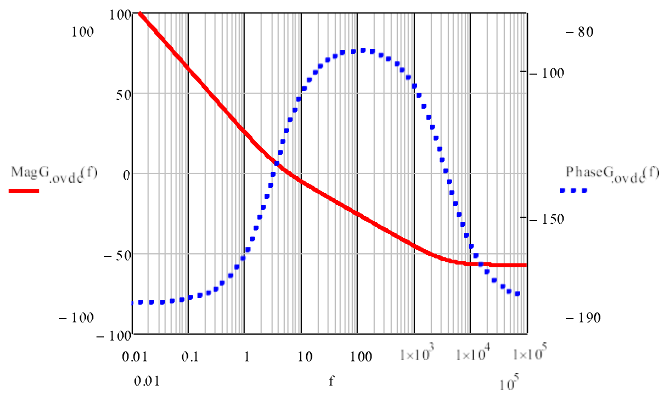

Fig. 9. Bode plot of the open loop dc-link voltage transfer function.

of the dc voltage control loop, consisting of a proportional integral compensator as in (34), where the parameters of k_p and k_i are the proportional and integral gains of the compensator, respectively,

$$G_{vdc}(s) = \frac{3v^{f}_{pcc,abc}}{2V_{dc}} \frac{1}{C_{dc}s}. \quad (32)$$

$$G_{ovdc}(s) = C_v(s)\, G_{vdc}(s) \quad (33)$$

$$C_v(s) = \frac{k_p s + k_i}{s}. \quad (34)$$

For DSP implementation of the dc-link voltage control scheme, $G_{vdc}(s)$, is converted from continuous plane "s" to the discrete plane "z" in (35). To allow the use of frequency response method design, the conversion of $G_{vdc}(z)$ transfer function from "z" plane to "w" plane in (36) is performed, using the bilinear transform of (23)

$$G_{vdc}(z) = \left(1 - z^{-1}\right) Z\left(\frac{G_{vdc}(s)}{s}\right). \quad (35)$$

$$G_{vdc}(w) = \frac{-0.00225w + 54}{w}. \quad (36)$$

The crossover frequency of the dc voltage loop is chosen to be $f_{cvdc} = 6$ Hz and the phase margin ϕ_{PMvdc} is selected to be 60°. We can compute that $k_p = 0.6$ and $k_i = 13.12$. Fig. 9 shows the frequency response of the open-loop dc-link voltage control scheme. It can be seen that at cross over frequency, the open loop gain of 0 dB and the phase margin of 60° are obtained.

The dc-link voltage controller $C_v(s)$ is also discretized for digital implementation using the bilinear transform with a sampling time of T_s that is also the switching period [24]. Therefore, the controller transfer function $C_v(z)$ can be expressed as follows:

$$C_v(z) = \frac{0.6z - 0.6}{z - 1}. \quad (37)$$

V. Real-Time Simulation and Hardware in the Loop Results

The proposed industrial system with the wind turbine shown in Fig. 1 was modeled and compiled using the well-known real-time simulator Opal-RT. Opal-RT allows precise benchmarking of real-time controllers, with specific sampling for specific control blocks. After an Opal-RT study such as this one, it is possible to generate C code for accurate compilation on real-time kernels or real-time operating systems, usually implemented with DSP hardware.

The PMSG parameters used in the model are taking from [25]. The specification of the wind turbine was selected in accordance to those parameters. The wind turbine has an optimum wind speed of 200 r/mIN at 10-m/s rated wind speed. The load parameters listed in Table II are used in the model.

The control algorithm was implemented using HIL. The wind turbine model with the grid connected back-to-back converter and power grid were built inside Matlab/Simulink. Then, the system was compiled inside the real-time simulator "Opal-RT." The control of the grid-side converter was implemented in the co-processor DSP (TI TMS230F28335), outside the Opal-RT system. The CPT theory was coded inside the DSP along with the current controllers. A sampling frequency of 12 kHz is used to discretize the signals. The test is implemented for various cases. The scaling for phase voltages, phase, and neutral currents per division are 60 V, 15 A and 5 A, respectively.

A. *Active Power Delivery*

In this case study, the four-leg inverter is set to deliver active power produced by the wind to the load, ($i_{ref} = i_{active}$), and the remaining active power is delivered to the grid with unity power factor without doing any compensation strategy. Fig. 10(a) shows the inverter voltage is in phase with the inverter current meaning only active power is delivered to the load and grid. From Fig. 10(b), the grid currents are unbalanced and distorted showing the requirement for power quality improvement. In Fig. 10(c), it is clear that the utility is supplying the linear and nonlinear single loads through its neutral wire while the inverter neutral current is zero.

B. *Active and Reactive Power Delivery*

In Fig. 11, the controller is set to supply the balance reactive current/power component of the load besides the delivery of active power ($i_{ref} = i_{active} + i^{b}$). From the voltage and current waveforms shown in Fig. 11(a), the inverter is supplying active and reactive power since the inverter current is no longer in phase with the voltage. The result of this compensation strategy is shown in Fig. 11(b) in which the void and unbalance current components of the load is supplied by the grid. It can be seen from Fig. 11(c) the grid is supplying the neutral current, related to single phase loads.

C. *Active Power Delivery and Unbalance Compensation*

The load considered in the system imposes unbalance component to the grid's current. Therefore, the CPT, proposed in the paper, is used to extract the unbalance current/power component of the load. In this study, the aim is to compensate the unbalance current component caused by the single- and intraphase loads ($i_{ref} = i_{active} + i^{u}$). Therefore, the inverter current is sinusoidal but unbalanced whereas the grid currents are

International journal of imaging science and engineering
ISSN: 1934--9955 www.ijise.net
Vol-20 Issue-01 Mar 2025

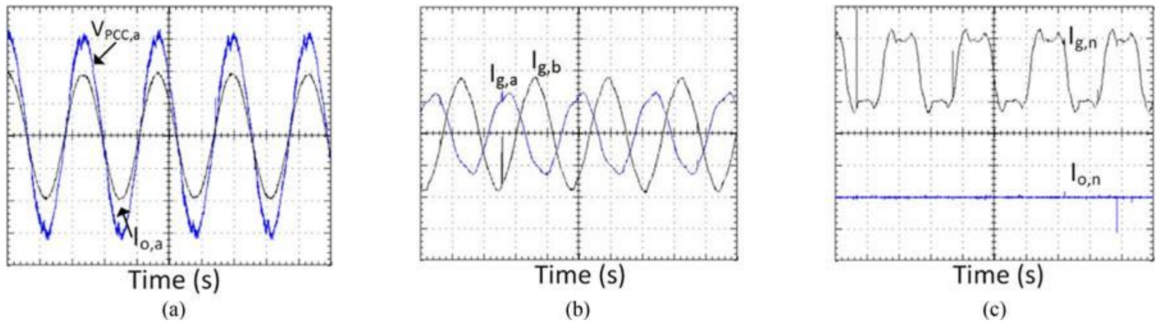

Fig. 10. Active power delivery: (a) PCC voltage and inverter current; (b) two phases of grid currents; and (c) grid neutral current ($I_{g,n}$) and inverter neutral current ($I_{o,n}$).

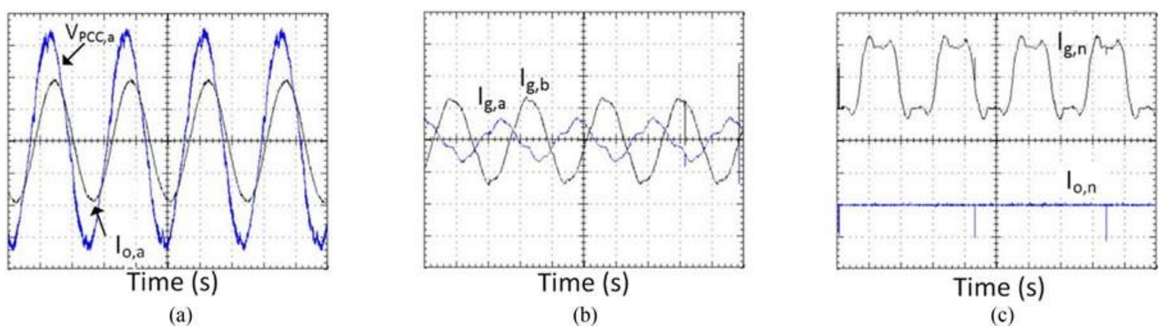

Fig. 11. Active and reactive power delivery: (a) PCC voltage and inverter current; (b) two phases of grid currents; and (c) grid neutral current ($I_{g,n}$) and inverter neutral current ($I_{o,n}$).

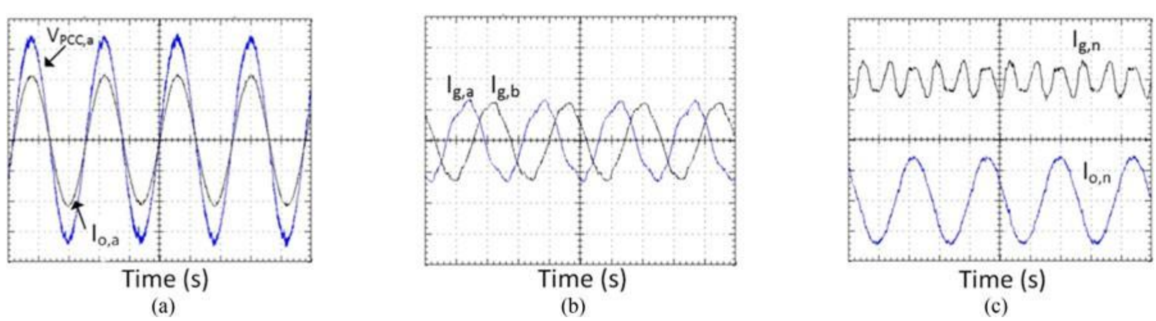

Fig. 12. Active power delivery and unbalance compensation: (a) PCC voltage and inverter currents; (b) two phases of grid current; and (c) grid neutral current ($I_{g,n}$) and inverter neutral current ($I_{o,n}$).

balanced but nonsinusoidal and out of phase with the voltages as shown in Fig. 12(a) and (b) respectively. In this case, the inverter current is responsible for supplying unbalance current component of the single phase loads through its fourth-leg as it is illustrated in Fig. 12(c). Note that the harmonic current component of the single- and three-phase loads is still supplied by the grid.

D. Active Power Delivery and Harmonics Compensation

At this case study, the inverter is providing harmonics compensation by injecting the void currents ($i_{\mathrm{ref}} = i_{\mathrm{active}} + i_v$). From Fig. 13(a) and (b), the inverter current is nonlinear whereas the grid current is sinusoidal but unbalanced and not in phase with the voltages. It can be observed that the grid in this case is not supplying the single-phase void current components through its neutral wire rather it is supplied by the inverter through its fourth-leg as illustrated in Fig. 13(c). The neutral wire of the grid caries only the unbalance current component related to the single-phase loads.

E. Active Power Delivery and Nonactive Compensation

In Fig. 14, the inverter is set to compensate nonactive current component of the load current including all disturbances, i.e., load reactive power, nonlinearities, and unbalances ($i_{\mathrm{ref}} = i_{\mathrm{active}} + i_{na}$). Fig. 14(a) shows that the inverter current contains nonactive current component, whereas Fig. 14(b) shows the gird is absorbing the remaining active current which is not consumed by the load. Note that the active current, exported

International journal of imaging science and engineering
ISSN: 1934--9955 www.ijise.net
Vol-20 Issue-01 Mar 2025

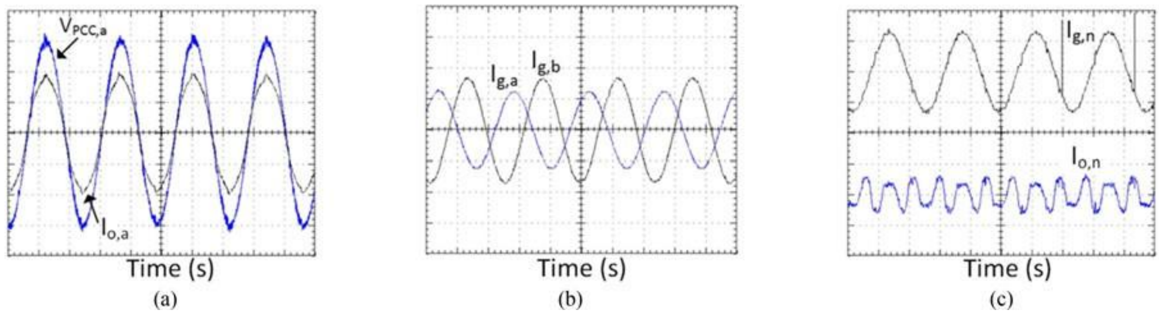

Fig. 13. Active power delivery and void compensation: (a) PCC voltage and inverter currents; (b) two phases of grid current; and (c) grid neutral current ($I_{g,n}$) and inverter neutral current ($I_{o,n}$).

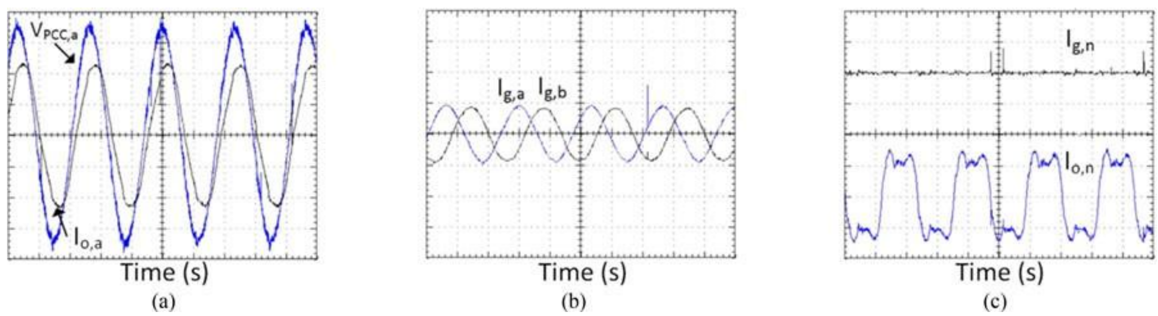

Fig. 14. Active power delivery and nonactive compensation: (a) PCC voltage and inverter currents; (b) two phases of grid current; and (c) grid neutral current ($I_{g,n}$) and inverter neutral current ($I_{o,n}$).

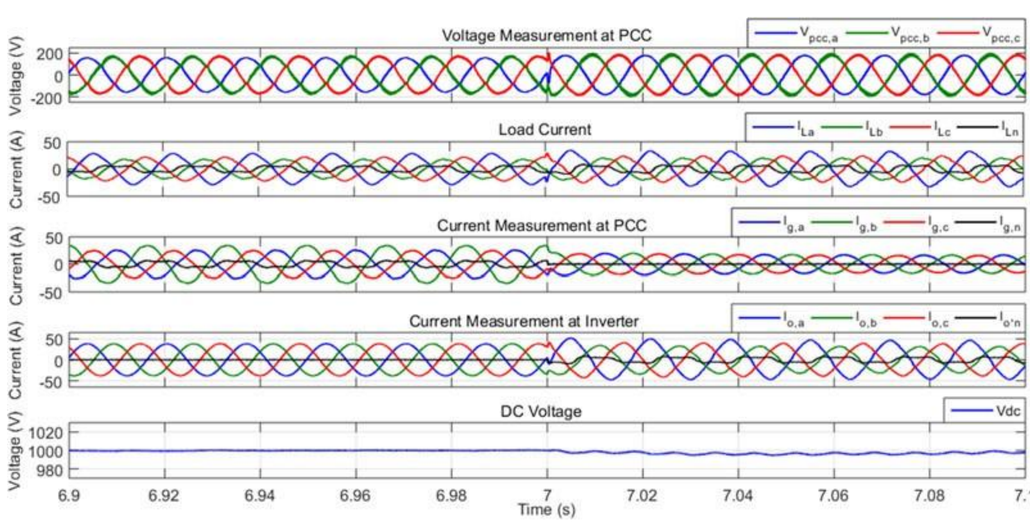

Fig. 15. Active power delivery and nonactive compensation at $t = 7$ s.

to the grid is proportional to the instantaneous PCC voltages. As shown in Fig. 14(c), the grid supplies zero current through its neutral and the inverter is supplying the return current of single phase loads through its fourth-leg.

F. Multifunctional and Active Filter Modes

In this section, two different tests are performed to validate the overall performance of the machine side and the grid side controllers during different wind speed conditions.

In Fig. 15, a test is done to validate the controller when it switches from active power delivery only to active and non-ctive compensation at maximum wind power. From Fig. 15, at $t = 7$ s, the inverter started providing active power as well as nonactive compensation. The dc-link voltage starts to oscillate but kept at its desired value. The grid current becomes sinusoidal and balanced. The inverter current, on the other hand, becomes unbalanced and nonlinear. The neutral current is produced by the fourth leg of the inverter resulting in zero neutral current at the grid side.

International journal of imaging science and engineering
ISSN: 1934--9955 www.ijise.net
Vol-20 Issue-01 Mar 2025

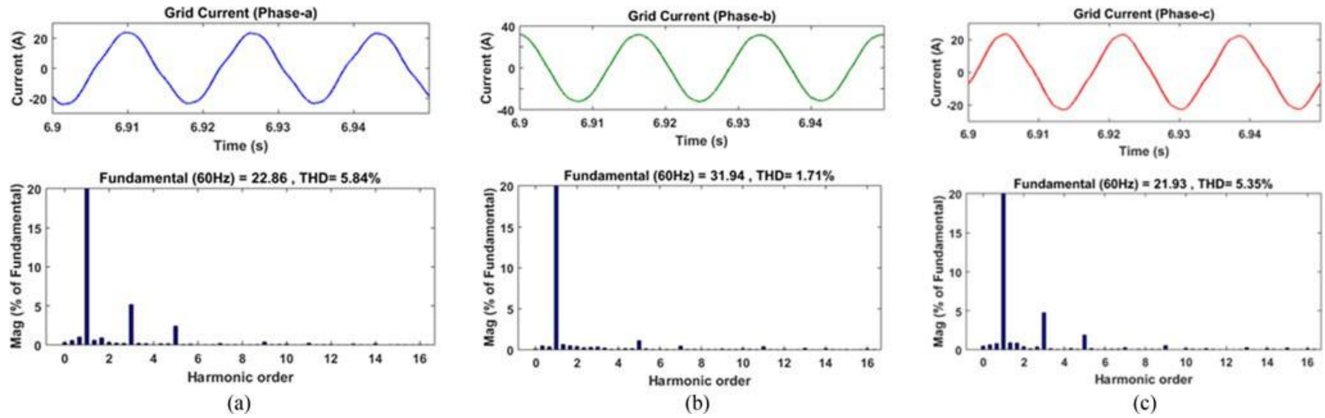

Fig. 16. Spectrum and THD of grid current without power quality improvement: (a) phase-a; (b) phase-b; and (c) phase-c.

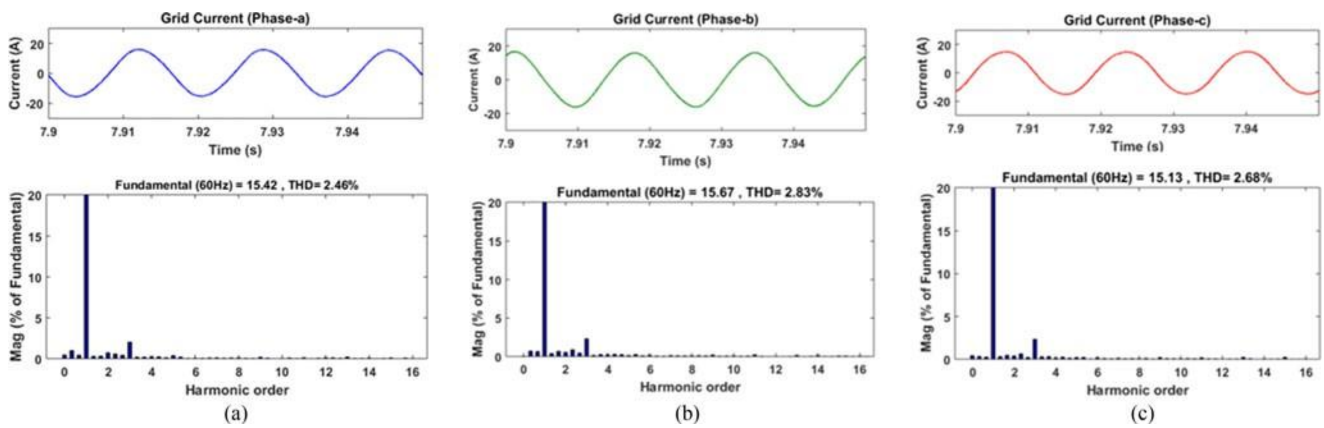

Fig. 17. Spectrum and THD of grid current with nonactive compensation: (a) phase-a; (b) phase-b; and (c) phase-c.

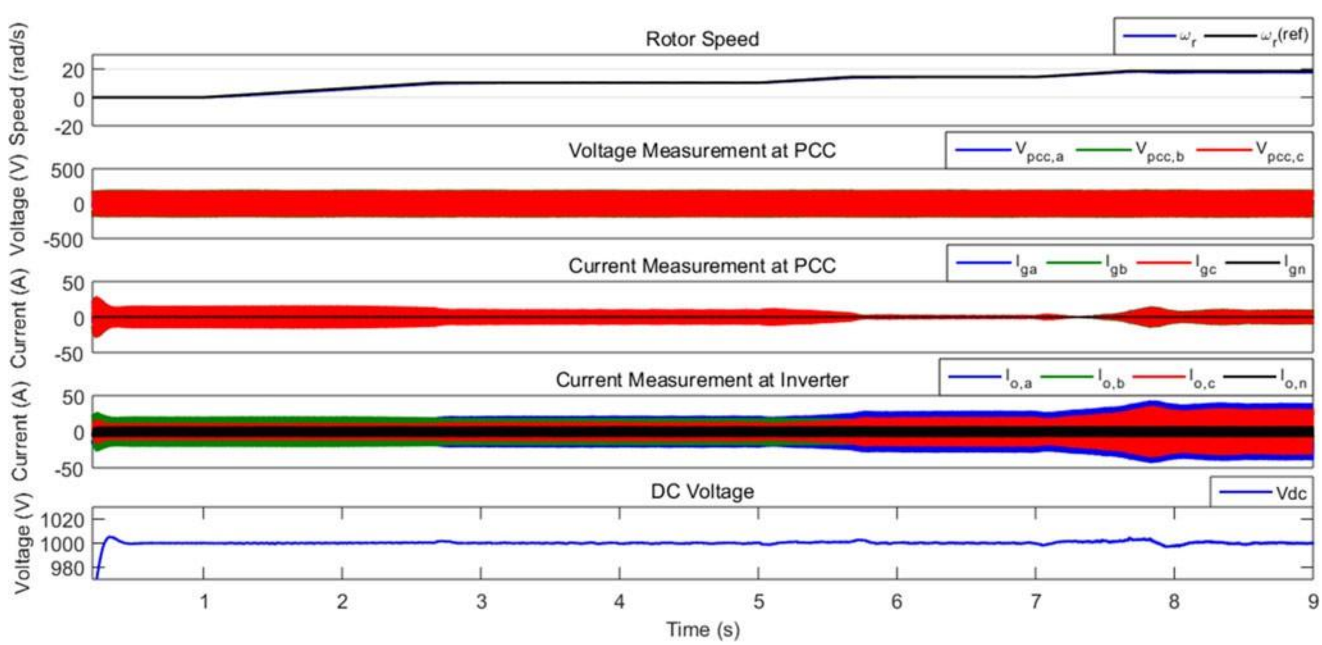

Fig. 18. Active power delivery and nonactive compensation under different wind speeds.

The harmonics spectrum of the grid current and total harmonic distortion (THD) with no compensation is shown Fig. 16. Since there are single- and three-phase loads as well as intraphase loads in the system, the THD is different for each phase. The current of phase-a and phase-c contain THD of 5.84% and 5.35%, respectively.

In Fig. 17, the grid current spectrum is demonstrated after the inverter is set to compensate the load nonactive current components. The THD of phases-a and phase-c were reduced from 5.84% and 5.35% to about 2.46% and 2.68%, respectively. Phase-b initially had much less harmonics because it does not have nonlinear single-phase load as the other phases. The amplitude of the grid current is reduced as the inverter is also supplying the unbalance components.

In Fig. 18, a comprehensive test is performed under different wind speeds. At no wind available or zero rotor speed, the grid-side inverter is operating as active filter. Therefore, the controller is intended to keep the dc voltage at constant value (1000 V) and provide nonactive compensation to improve the power quality of the grid current. During this condition, the grid supplies the active power for the load. When the wind speed increases above the cut-in speed and the turbine started producing power, the grid-side inverter inject the active and compensate nonactive components. If the produced power is more than the load power, the remaining is injected to the grid. During all the time, the dc-link voltage is kept constant at 1000 V.

VI. Conclusion

This paper addressed a comprehensive control method for a back-to-back wind turbine system connected to an industrial plant. The control uses the four-leg inverter at the grid side to supply available active power from the wind turbine system along with full compensation of load current disturbances. The main contribution is based on CPT to impress the set-point reference and impose disturbances mitigation, which adds significant flexibility to the control structure.

The control structure was tested with a comprehensive real-time benchmarking case-study with hardware in the loop. The control algorithms were compiled inside our TI DSP and validated using the real-time system "Opal-RT." The algorithms were debugged and are ready for experimental validation in a retrofitting of a wind turbine (future work). The results showed good performance of the algorithm and the THD was improved for all different operation conditions. The results support the system presented here which can avoid installation of active filter hardware by the utility or by the industrial consumer.

References

[1] "Global wind report annual market update 2013," 2013. [Online]. Available: http://www.gwec.net

[2] S. Li, T. A. Haskew, R. P. Swatloski, and W. Gathings, "Optimal and direct-current vector control of direct-driven PMSG wind turbines," *IEEE Trans. Power Electron.*, vol. 27, no. 5, pp. 2325–2337, May 2012.

[3] N. Angela, M. Liserre, R. A. Mastromauro, and A. D. Aquila, "A survey of control issues in PMSG-based," *IEEE Trans. Ind. Informat.*, vol. 9, no. 3, pp. 1211–1221, Aug. 2013.

[4] J. Lagorse, M. G. Simo˜es, and A. Miraoui, "A multiagent fuzzy-logic-based energy management of hybrid systems," *IEEE Trans. Ind. Appl.*, vol. 45, no. 6, pp. 2123–2129, Nov./Dec. 2009.

[5] X. Tan, Q. Li, and H. Wang, "Advances and trends of energy storage technology in microgrid," *Int. J. Elect. Power Energy Syst.*, vol. 44, pp. 179–191, Jan. 2013.

[6] P. F. Ribeiro, B. K. Johnson, M. L. Crow, A. Arsoy, and Y. Liu, "Energy storage systems for advanced power applications," *Proc. IEEE*, vol. 89, no. 12, pp. 1744–1756, Dec. 2001.

[7] M. G. Simoes, B. K. Bose, and R. J. Spiegel, "Fuzzy logic based intelligent control of a variable speed cage machine wind generation system," *IEEE Trans. Power Electron.*, vol. 12, no. 1, pp. 87–95, Jan. 1997.

[8] A. Chauhan and R. P. Saini, "A review on integrated renewable energy system based power generation for stand-alone applications: Configurations, storage options, sizing methodologies and control," *Renew. Sustain. Energy Rev.*, vol. 38, pp. 99–120, Oct. 2014.

[9] C. N. Bhende, S. Mishra, and S. G. Malla, "Permanent magnet synchronous generator-based standalone wind energy supply system," *IEEE Trans. Sustain. Energy*, vol. 2, no. 4, pp. 361–373, Oct. 2011.

[10] H. Akagi, E. H. Watanabe, and M. Aredes, "Instantaneous power theory and applications to power conditioning," *IEEE Industrial Electron. Magazine*, vol. 1, no. 3, p. 46, Fall 2007.

[11] P. Tenti, H. K. M. Paredes, and P. Mattavelli, "Conservative power theory, a framework to approach control and accountability issues in smart microgrids," *IEEE Trans. Power Electron.*, vol. 26, no. 3, pp. 664–673, Mar. 2011.

[12] A. Mortezaei, M. G. Simoes, and F. P. Marafao, "Cooperative operation based master-slave in islanded microgrid with CPT current decomposition," in *Proc. IEEE Power Energy Gen. Meeting*, Denver, CO, USA, 2015, pp. 1–5.

[13] A. Mortezaei, C. Lute, M. G. Simo˜es, F. P. Marafa˜o, and A. Boglia, "PQ, DQ and CPT control methods for shunt active compensators – a comparative study," in *Proc. Energy Convers. Congr. Expo*., 2014., pp. 2994–3001.

[14] A. Mortezaei, M. G. Simoes, T. D. Busarello, and A. Al Durra, "Multifunctional strategy for four-leg grid-tied DG inverters in three-phase four-wire systems under symmetrical and asymmetrical voltage conditions," in *Proc. 12th IEEE/IAS Int. Conf. Ind. Appl.*, Curitiba, Brazil, Nov. 2016, pp. 1–8.

[15] V. Khadkikar, A. Chandra, and B. Singh, "Digital signal processor implementation and performance evaluation of split capacitor, four-leg and three H-bridge-based three-phase four-wire shunt active filters," *IET Power Electron*., vol. 4, no. 4, pp. 463–470, Apr. 2011.

[16] Z. Liu, J. Liu, and J. Li, "Modelling, analysis, and mitigation of load neutral point voltage for three-phase four-leg inverter," *IEEE Trans. Ind. Electron.*, vol. 60, no. 5, pp. 2010–2021, May 2013.

[17] L. B. Garcia Campanhol, S. A. Oliveira Da Silva, and A. Goedtel, "Application of shunt active power filter for harmonic reduction and reactive power compensation in three-phase four-wire systems," *IET Power Electron*., vol. 7, no. 11, pp. 2825–2836, Nov. 2014.

[18] M. BarghiLatran, A. Teke, and Y. Yoldas, "Mitigation of power quality problems using distribution static synchronous compensator: A comprehensive review," *IET Power Electron*., vol. 8, no. 7, pp. 1312–1328, Jul. 2015.

[19] A. Mortezaei, M. G. Simoes, M. Savaghebi, J. M. Guerrero, and A. Al Durra, "Cooperative control of multi-master-slave islanded microgrid with power quality enhancement based on conservative power theory," *IEEE Trans. Smart Grid*, pp. 1–12, Nov. 2016. DOI: 10.1109/TSG.2016.2623673.

[20] A. S. Bubshait, M. G. Simo˜es, A. Mortezaei, and T. D. C. Busarello, "Power quality achievement using grid connected converter of wind turbine system," in *Proc. 51st Annu. Meeting IEEE Ind. Appl. Soc.*, 2015, pp. 1–8.

[21] Z. Lubosny, *Wind Turbine Operation in Electric Power Systems*. New York, NY, USA: Springer, 2003.

[22] M. G. Simo˜es *et al.*, "Interactive smart battery storage for a PV and wind hybrid energy management control based on conservative power theory," *Int. J. Control*, vol. 89, no. 4, pp. 1–50, Oct. 2015.

[23] A. Yazdani and R. Iravani, *Voltage-Sourced Converters in Power Systems: Modeling, Control, and Applications*. Hoboken, NJ, USA: Wiley, 2010.

[24] A. Mortezaei *et al.*, "Multifunctional control strategy for asymmetrical cascaded H-bridge inverter in microgrid applications," *IEEE Trans. Ind. Appl.*, pp. 1–14, Nov. 2016. DOI: 10.1109/TIA.2016.2627521.

[25] Y. Xia, K. H. Ahmed, and B. W. Williams, "A new maximum power point tracking technique for permanent magnet synchronous generator based wind energy conversion system," *IEEE Trans. Power Electron.*, vol. 26, no. 12, pp. 3609–3620, Dec. 2011.

Abdullah S. Bubshait (S'13) received the B.Sc. degree in electrical engineering from the King Fahd University of Petroleum and Minerals, Dhahran, Saudi Arabia, and the M.Sc. degree in electrical engineering from the University of Calgary, Calgary, AB, Canada, in 2005 and 2011, respectively. He is currently working toward the Ph.D. degree in the Department of Electrical Engineering and Computer Science, Colorado School of mines, Golden, Co, USA.

In 2011, he joined the Department of Electrical Engineering at King Faisal University, Hofuf, Saudi Arabia, as a Lecturer, where since 2013, he has been with the Center for the Advanced Control of Energy and Power Systems. His research interests include design, control and modeling of power electronics to renewable energy resources for photovoltaics, and wind turbines.

Ali Mortezaei (S'14) received the M.Sc. degree in electrical engineering from the Colorado School of Mines (CSM), Golden, CO, USA, in 2015, where he is currently working toward the Ph.D. degree in electrical engineering.

He has been with the Center for the Advanced Control of Energy and Power Systems, CSM, since 2013. His main research interests include active power filters, power quality, multilevel inverters, distributed compensation strategies, and microgrids.

Mr. Mortezaei received the Outstanding Research Award in 2016 from the Department of Electrical Engineering and Computer Science, CSM.

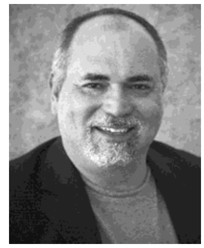

Marcelo Godoy Simo˜es (F'16) received the B.Sc. and M.Sc. degrees in electrical engineering from the University of Sao Paulo, Sao Paulo, Brazil, in 1985 and 1990, respectively; the Ph.D. degree in electrical engineering from the University of Tennessee, Knoxville, TN, USA in 1995; and the D.Sc. degree (Livre-Docencia) in mechanical engineering from the University of Sao Paulo in 1998.

He is a pioneer in applying neural networks and fuzzy logic in power electronics, motor drives, and renewable energy systems. His fuzzy logic-based modeling and control for wind turbine optimization is used as a basis for advanced wind turbine control and it has been cited worldwide. His leadership in modeling fuel cells is internationally and highly influential in providing a basis for further developments in fuel cell automation control in many engineering applications. He made substantial and lasting contributions in artificial intelligence technology in many applications, power electronics and motor drives, fuzzy control of wind generation system such as fuzzy Logic-based waveform estimation for power quality, neural network-based estimation for vector controlled motor drives, and integration of alternative energy systems to the electric grid through artificial intelligence modeling-based power electronics control.

Dr. Simo˜es was an U.S. Fulbright Fellow for academic year 2014–15 from Aalborg University, Institute of Energy Technology, Aalborg, Denmark.

Tiago Davi Curi Busarello (S'13–M'15) received the bachelor's degree in electrical engineering from Santa Catarina State University, Trindade, Brazil, in 2010, and the M.Sc. and Ph.D. degrees in electrical engineering from the University of Campinas, Campinas, Brazil, in 2013 and 2015, respectively.

Since 2016, he has been a Professor with the Federal University of Santa Catarina, Campus Blumenau, Brazil. He conducts researches with the Center for Advanced Control of Energy and Power Systems, University Colorado School of Mines, Golden, CO, USA. His areas of interest include power electronics and smart grids.

Dr. Busarello is a member of the IEEE Power and Energy Society and the IEEE Power Electronics Society.